RESEARCH ARTICLE

Optical spinning rheometry test on viscosity curves of less viscous fluids at low shear rate range

Daisuke Noto[1] · Kohei Ohie[2] · Taiki Yoshida[3] · Yuji Tasaka[2]

Abstract

We propose a method, named optical spinning rheometry (OSR), to acquire kinematic viscosity curves of Newtonian and non-Newtonian fluids in the same framework. The OSR is independent of torque measurements and utilizes velocity information measured by particle tracking velocimetry. This optical approach enables flexibility in velocity resolution, and benefits exploring the low shear rate region. In addition, the kinematic viscosity of less viscous fluids like water or dilute polymer solutions can be assessed as being free from the mechanical limitations of torque sensors. The applicable range of the OSR is discussed in detail, and its performance is verified in Newtonian fluids. Demonstrations in dilute xanthan gum solutions, concentrations of $O(10\ \mathrm{ppm})$, show the capability of measuring their shear-thinning behaviors and the kinematic viscosity curves even in the first Newtonian regime.

1 Introduction

Rheological behaviors of non-Newtonian fluids are relevant for a broad range of fields, including polymer, biology, food processing, and of course, fluid mechanics (e.g., Barnes et al. 1989). For instance, in the field of fluid mechanics, it is well-known that tiny additives of high molecular-weight polymers or surfactants to Newtonian fluids significantly reduce turbulent frictional drag, even at concentrations on the order of a few ppm (Sureshkumar et al. 1997; Den Toonder et al. 1997; Dimitropoulos et al. 2001; Min et al. 2003; Escudier et al. 2009). Thanks to the recent development of computational power, complex fluid motions of non-Newtonian fluids have been examined via numerical approaches (Alves et al. 2021). In numerical simulations, rheological behaviors of non-Newtonian fluids need to be represented by constitutive equations, such as power law model, Cross model, Carreau–Yasuda model, and so on (Abbasian et al. 2020), in order to couple the rheological properties with the momentum conservation equation. The constitutive equations have to be based on direct measurements of the material properties using rheometers when considering non-Newtonian fluids that truly exist in nature.

A rheometer is, in general, efficient to measure rheological properties of non-Newtonian fluids, such as viscosity and elasticity. The primary measure of standard rheometers is, however, not stress and strain. Instead, torque or angle displacement (angular velocity) is measured via mechanical sensors and these are converted to rheological properties through various assumptions of the measurement systems. Apparently, it is not straightforward to directly measure stress or strain of non-Newtonian fluids using rheometers, as flow fields are not self-evident. In some cases, discrepancies between the assumptions held for rheometer and actual flow fields within the interrogation domain cause large deviations or errors in the measurements of rheological properties (Hyun et al. 2011; Ewoldt et al. 2015). For such a case, a proper correction method like the Weissenberg–Rabinowitsch–Mooney correction is applied to prevent false rheological properties (Macosko 1994). However, this kind of correction is empirical and not universally applied to unknown fluid properties. There are different approaches to overcome this issue with the help of velocity field measured by supplemental velocimetry such as particle image velocimetry (PIV), and it is known as Rheo-PIV (e.g., Dimitriou et al. 2011; Serrano-Aguilera et al. 2016; Medina-Bañuelos

✉ Daisuke Noto
  dnoto@sas.upenn.edu

1 Department of Earth and Environmental Science, University of Pennsylvania, Philadelphia, USA

2 Laboratory for Flow Control, Faculty of Engineering, Hokkaido University, Sapporo, Japan

3 National Institute of Advanced Industrial Science and Technology, Tsukuba, Japan

et al. 2019). The actual flow field of the measurement domain has to be monitored to prevent misinterpretation of the obtained data. Otherwise, virtual rheological properties can be produced by non-ideal flows like slip, shear-banding, and so on.

A requirement from numerical and analytical studies is to obtain viscosity (or flow) curves across a wide range of shear rate $\dot{\gamma}$, from zero to infinite shear, because of the necessity to build constitutive equations for representing the rheological properties of interest. It is a must to pay attention to the measurable range of the rheometer based on both the mechanical limitations of torque sensors and the flow fields to avoid spurious data (Ewoldt et al. 2015). Lower shear rate region, the mechanical limitation of the installed torque sensor can be a bottleneck, as the measurable range needs to satisfy the following relation

$$\tau = \mu\dot{\gamma} \geq F_\tau M_{\min}, \tag{1}$$

where τ, μ, and $\dot{\gamma}$ are the shear stress, the dynamic viscosity, and the shear rate, respectively. Whereas F_τ is the geometrical parameter and $M_{\min}$ is the minimum torque that can be measured by the sensor, and these two are unique to each rheometer. Since the torque limit $M_{\min}$ is prescribed for each rheometer, the lower limit of the shear rate is sometimes hard to adjust especially for less viscous fluids. In addition to the lower limit, the upper limit of the shear rate is also constrained by the emergence of secondary flows such as the Taylor vortices. This is not due to mechanical limitation, but is determined by a physical phenomenon itself and might be hard to control especially for less viscous fluids. Therefore, it is challenging to measure less viscous fluids, whose viscosity is close to that of water. Hence, a novel rheometry that is independent of torque sensors is highly required to expand the viscosity curves of less viscous fluids into low shear rate regions.

Under these circumstances, Tasaka et al. (2015) proposed a novel concept of rheometry based on velocity information measured using ultrasonic velocity profiling (UVP). The methodology, termed ultrasonic spinning rheometry (USR), is a kinematic rheometry and solves the equation of motion by substituting the velocity information measured in an oscillatory shear flow, and as a result, shear-rate-dependent viscosity is possible to be obtained from a single measurement. The concept of the USR is on the basis of a dynamical approach, which differs from a kinematic approach used in the standard rheometers. Thus, the USR can quantify ongoing physical properties caused by the flow itself. The USR was originally proposed as a viscometry for a bubbly fluid in Tasaka et al. (2015), and it allows expanding its functionalities to measure more complicated rheological properties (Yoshida et al. 2017, 2018, 2019; Ohie et al. 2022). The USR, however, has one

limitation; it cannot access the low shear rate region due to the small dynamic range of the velocity of the UVP as discussed briefly in Yoshida et al. (2022).

In this paper, we present a novel method of kinematic rheometry which measures the shear-rate-dependent viscosity of fluids throughout an optical approach. The proposed method couples the idea of the USR with the particle tracking velocimetry (PTV) to widen the dynamic range of velocity to expand the shear rate range of the viscosity curves. Following the introduction, Sect. 1, the concept and its implementation are described in Sect. 2. The efficacy of the proposed methodology is verified using Newtonian fluids in Sect. 3. Application of the methodology to polymer solutions is presented in Sect. 4. A summary of the main outcomes of this study is provided in Sect. 5.

2 Optical spinning rheometry (OSR)

2.1 Theoretical basis of spinning rheometry

Building on UVP measurements, Tasaka et al. (2015) introduced the fundamentals for USR to characterize the effective viscosity of bubble suspensions. Extensions of the USR have been explored in non-Newtonian fluids using UVP to enable velocity field measurements even in opaque liquids. The efficacy of the USR has been already proved by comparing it with a standard rheometer (Yoshida et al. 2019). Thus, only key features are described here.

Consider a cylinder of radius R that oscillates sinusoidally along the azimuth. The temporal change of the azimuthal velocity at the cylindrical wall can be written as $u_{\mathrm{wall}}(t) = U_{\mathrm{wall}} \sin(2\pi f_\mathrm{o} t)$, where U_{wall} and f_o are the maximum wall velocity and the oscillation frequency. As long as the flow remains laminar, the flow field inside the oscillating cylinder can be assumed as axisymmetric and unidirectional in the azimuthal direction. Under the above assumption, the azimuthal component of the equation of motion for Newtonian fluid in a cylindrical system reduces to

$$\frac{\partial u_\theta}{\partial t} = \nu \left(\frac{\partial^2}{\partial r^2} + \frac{1}{r}\frac{\partial}{\partial r} - \frac{1}{r^2} \right) u_\theta, \tag{2}$$

where ν is the kinematic viscosity of the fluid. Consideration of separation of variable on t and r, the radial component of Eq. 2 admits exact Bessel solutions for a given ν (e.g., Tasaka et al. 2015, 2018; Song and Rau 2020). Imposing two boundary conditions at the wall, $u_\theta(r = R, t) = u_{\mathrm{wall}}(t)$, and at the center, $u_\theta(r = 0, t) = 0$, the solution of Eq. 2 is derived for a fixed kinematic viscosity ν as

$$u_\theta(r, t; \nu) = U(r; \nu) \sin \left[2\pi f_\mathrm{o} t + \phi(r; \nu) \right], \tag{3}$$

where $U(r; \nu)$ and $\phi(r; \nu)$ are, respectively, radial distributions of the velocity amplitude and the phase lag with

$U(r = R) = U_{\text{wall}}$. The azimuthal momentum is transported from the forced cylindrical wall toward the center accompanied by phase lag $\phi(r)$. The phase lag distribution in experiments $\phi_e(r)$ is then acquired by measurement, and its slope (radial gradient) $\phi'_e(r)$ is computed. The phase lag ϕ can also be analytically derived for a given ν as

$$\phi(r;\nu) = \tan^{-1}\left[\frac{\Phi(R)\Psi(r) - \Phi(r)\Psi(R)}{\Phi(R)\Phi(r) + \Psi(R)\Psi(r)}\right], \tag{4}$$

where $\Phi(r)$ and $\Psi(r)$ are series and their detailed derivations are described in Tasaka et al. (2015). By matching the local phase lag gradient $\phi'_e(r)$ and those obtained from the analytic solutions $\phi'(r;\nu)$ for a given ν range, the effective viscosity ν_{eff} is found as ν must satisfy $\phi'_e(r) = \phi'(r;\nu)$ at each radial position. It is thus possible to obtain the radial distribution of the effective viscosity $\nu_{\text{eff}}(r)$ by computing analytically $\phi'(r;\nu)$. In addition, shear rate distributes in the radial direction according to the effective local fluid deformation caused by the sinusoidal forcing. A standard torque rheometer assumes a constant shear rate in its narrow measurement section and evaluates shear-rate-dependent viscosity by a shear rate sweep test. In contrast, the OSR enables a rapid characterization with only one set of control parameters as it allows spatial variations of shear rate and viscosity in the cylinder.

2.2 Experimental design

A drawback of the USR is its dynamic range in shear rate, as the velocity and spatial resolutions rely on the specification of the UVP, and they are typically in $O(1 \text{ mm/s})$ and $O(1 \text{ mm})$. In the case of a less viscous fluid like water, the Reynolds number $Re = U_{\text{wall}}R/\nu$ easily exceeds laminar conditions, even with a maximum velocity $U_{\text{wall}} = O(1 \text{ mm/s})$ and a thickness of the viscous layer $\delta_\nu = O(0.1 \text{ mm})$ for this oscillation condition. These device-dependent limitations do not allow measuring small kinematic viscosities which may be achieved at low shear rates $\dot{\gamma} \leq O(10^{-1} \text{ s}^{-1})$. To overcome this constraint, this study puts forth utilizing PTV to reconstruct the velocity field. In principle, the velocity resolution of PTV has no limitations as long as seeding particles can trace the flow field between consecutive time intervals. The spatial resolution of PTV is considered as the size of seeding particles, i.e., $O(10^1–10^2 \text{ µm})$, which surpasses the spatial resolution of the UVP. In addition to this, PTV can define arbitrary time intervals between consecutive images, and decades of velocity magnitude can be quantified in a single experiment. This optical approach, hereafter optical spinning rheometry (OSR), thus can surpass the limitation of the USR even though the test fluids need to be transparent enough for visualization. Since the spinning rheometry is based only

on the velocity information, it is possible to apply the same analytic procedure for the OSR.

We specifically designed an experimental apparatus to fulfill the assumptions of the spinning rheometry, which allows any optical approaches such as PTV and PIV, detailed in Sect. 2.1. The apparatus has a triple-wall construction comprised of a rectangular tank, a cylindrical tank, and an oscillating cylinder. All the walls are made of transparent acrylic materials. A schematic view of the experimental system is illustrated in Fig. 1; top and side views are shown in Fig. 1a and b, respectively. The outer rectangular tank enables the circulation of temperature-controlled water supplied from a thermostatic bath. As well as it allows keeping the temperature constant, minimizes optical deflections arising from the curvatures of the cylindrical wall and uniform lighting is possible even in the cylindrical geometries. The cylindrical tank, which is composed of a 3-mm-thick annulus and a flat bottom plate, contains the test fluid, and it is placed at the center of the rectangular tank. The oscillating cylinder is comprised of a cylindrical annulus with an internal
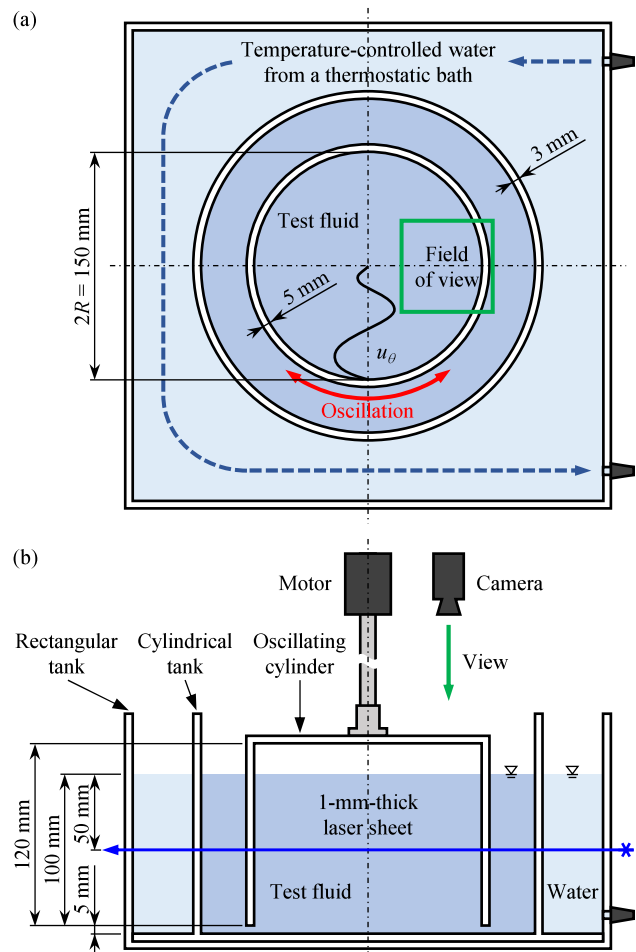

Fig. 1 Schematics of the experimental apparatus for the optical spinning rheometry (OSR): **a** top view and **b** side view

radius of $R = 75$ mm, a height of 120 mm, and a thickness of 5 mm, and a transparent top plate. The center of the top plate is supported by a stainless rod connected to a stepper motor mounted above, and the rotational axis coincides with the center of the cylindrical tank. Note that there is a 5-mm gap between the rim of the oscillating cylinder and the bottom of the cylindrical tank, and this reduces the influence of Ekman pumping leading to meridional flows. Levels of the temperature-controlled water and the test fluid were set to 105 mm, and thus, the measurement section, i.e., the internal region of the oscillating cylinder at which the assumption of axisymmetric and unidirectional flow holds , was a column with a diameter of $2R = 150$ mm and height of 100 mm.

Oscillation of the cylinder was controlled by the motor to have a sinusoidal azimuthal velocity $u_{wall}(t) = U_{wall} \sin(2\pi f_o t)$, where f_o is the oscillation frequency. Controlling an oscillation angle $\pm\Theta$ from the original position, the maximum wall velocity becomes $U_{wall} = 2\pi f_o R\Theta$. The surfaces of the fluids were opened to air at room temperature meaning free-slip boundaries, while the others are no-slip. Thanks to the temperature-controlled water circulating around, the temperature of the test fluid during measurements can be kept arbitrarily constant, typically from $T \sim 5\,°C$ to $50°C$ with an accuracy of $\pm 0.3°C$. The temperature of the test fluid was directly measured before and after each measurement using a thermometer.

Spherical resin particles of mean diameter $d_p \sim 100$ μm were seeded into the test fluid for the tracer of PTV. The specific gravity of the particles is close to unity in each test fluid, and this minimized the buoyancy effect. A 500-mW continuous blue laser sheet with a thickness of 1 mm illuminated the horizontal (r-θ) plane at 50 mm beneath the surface. Velocity fields of the oscillatory flows were measured using an in-house PTV code based on the nearest neighbor method, whose robustness was demonstrated in Noto et al. (2021a, b). It is worth emphasizing that PTV is preferable over PIV for the following reasons. One is that the addition of dense seeding particles for allowing PIV may change the physical properties of the test fluids (e.g., Mader et al. 2013). Since the present method aims to measure less viscous fluids like water or dilute polymer solutions with a concentration in the order of ppm, the seeding density of particles needs to be negligible. The other is that PTV has a better spatial resolution and avoids the spatial smoothing effect of PIV arising in setting interrogation windows. This effect blurs fluid deformation leading to an underestimation of the shear rate. PTV is therefore employed to measure velocity distribution; the seeding density of the particles was kept less than 1 ppm for all the measurements. To focus on the viscous boundary layer formed on the oscillatory internal cylindrical boundary, the field of view is fairly closed up to the wall, i.e., the camera does not capture the whole cylindrical region. The effective survey window covers typically the area of

$0.3 \le r/R \le 1.0$ and $-\pi/4 \le \theta \le \pi/4$. This is because the viscous layer of less viscous fluids can become extremely thin, as shown by the Stokes' first (Rayleigh) problem,

$$\delta_v = \sqrt{\frac{\nu}{\pi f_o}}. \tag{5}$$

It is worth noting that the f_o is not a fully arbitrary parameter and needs to be set carefully so as to let δ_v be in the range of $d_p < \delta_v < R$ as a rough estimate. The lower limit is the spatial resolution of the PTV. The upper limit ensures the emergence of the phase lag; otherwise, the viscosity information appeared as the phase lag will be hidden due to the immediate development of rigid-body rotation. For water at room temperature, the δ_v values are estimated as 1–10 mm with $f_o = 0.01$–1 Hz. Besides this limitation, there are other factors to be considered in advance of the measurements, and these are summarized in Sect. 2.4.

2.3 Analytic procedures

The process chart in Fig. 2 summarizes the analytical and experimental procedures proposed to characterize effective viscosity. The two main streams are done separately and merged at the end of the procedures to compute kinematic viscosity of test fluids.

First azimuthal velocity fields as a function of radius and time, $u_\theta(r, t)$, need to be acquired using PTV. As the field of view does not contain the central position of the oscillating cylinder (Fig. 1a), the center and the wall positions are identified from the wall location estimated from the particle
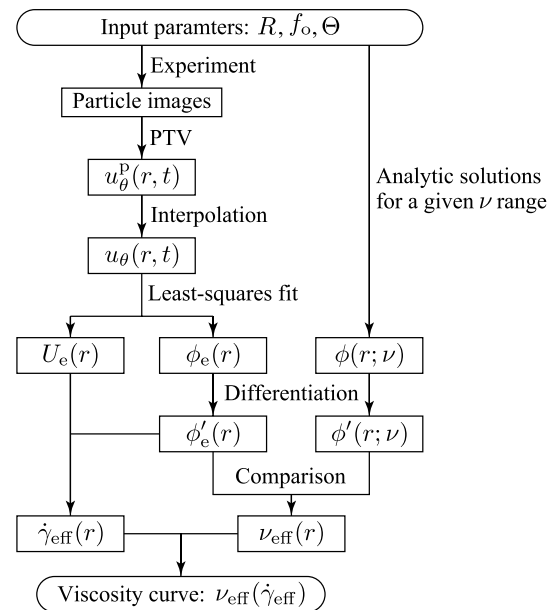

Fig. 2 Process chart of the OSR to obtain viscosity curves

images adhered or close (reflected) to the cylindrical wall. The central position is possible to find through the least-squares fit for the identified wall location; a similar approach was done earlier by Song and Rau (2020). Figure 3 illustrates an example of the identified cylindrical wall and its center positions on a particle pathline image. The pathline image is inverted for better visibility, and an enlarged view of the region enclosed by a blue square is shown in the inset. From the pathline image, it is easy to recognize the adhered particles on the cylindrical wall as these appear as a mirror
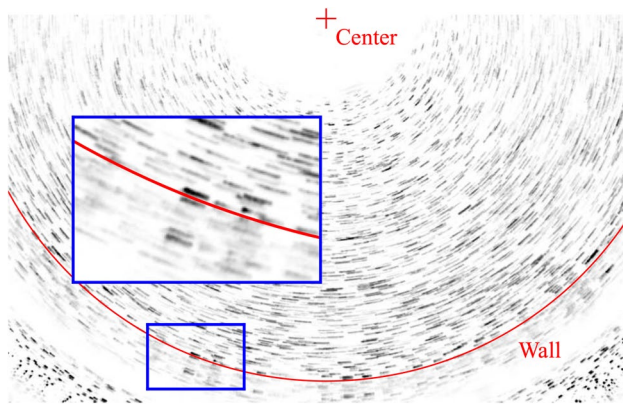
image on the wall. The measurement domain thus can be determined as an internal region of the identified wall.

Hence, azimuthal velocities of the seeding particles with their radial positions $u_\theta^{\mathrm{p}}(r, \theta; t)$ are obtained at each particle position. Please note that the lens aberration is not corrected in the present study as a lens with a long focal length was employed and its effect may be negligible. It is, however, possible to directly calibrate the image positions to the real positions throughout a standard calibration process, and this process is necessary when a larger cylinder, which can lead to a strong lens aberration, is employed.

To obtain a radial distribution of azimuthal velocity at a specific moment $u_\theta(r; t)$, the Shepard interpolation (Shepard 1968) is applied to the randomly distributed velocity information measured by PTV building on the radial positions of the particles r_i as

$$\langle u_\theta(r; t)\rangle_\theta = \frac{\sum_i^{N_{\mathrm{p}}} |r - r_i|^{-2} u_\theta^{\mathrm{p}}(r_i; t)}{\sum_i^{N_{\mathrm{p}}} |r - r_i|^{-2}}, \tag{6}$$

where N_{p} is the number of particles existing in a concentric region $|r - r_i| \leq \Delta r$ with Δr as a grid interval of the interpolation. Notice that $\langle u_\theta(r; t)\rangle_\theta$ is an azimuthally averaged azimuthal velocity at a specific moment t, and this is written $u_\theta(r; t)$ hereafter for readability. Thanks to this interpolation that uses the squares of the inverse distance as the weight, measurement noise is minimized while suppressing undesired smoothing in the radial direction, and derivatives can
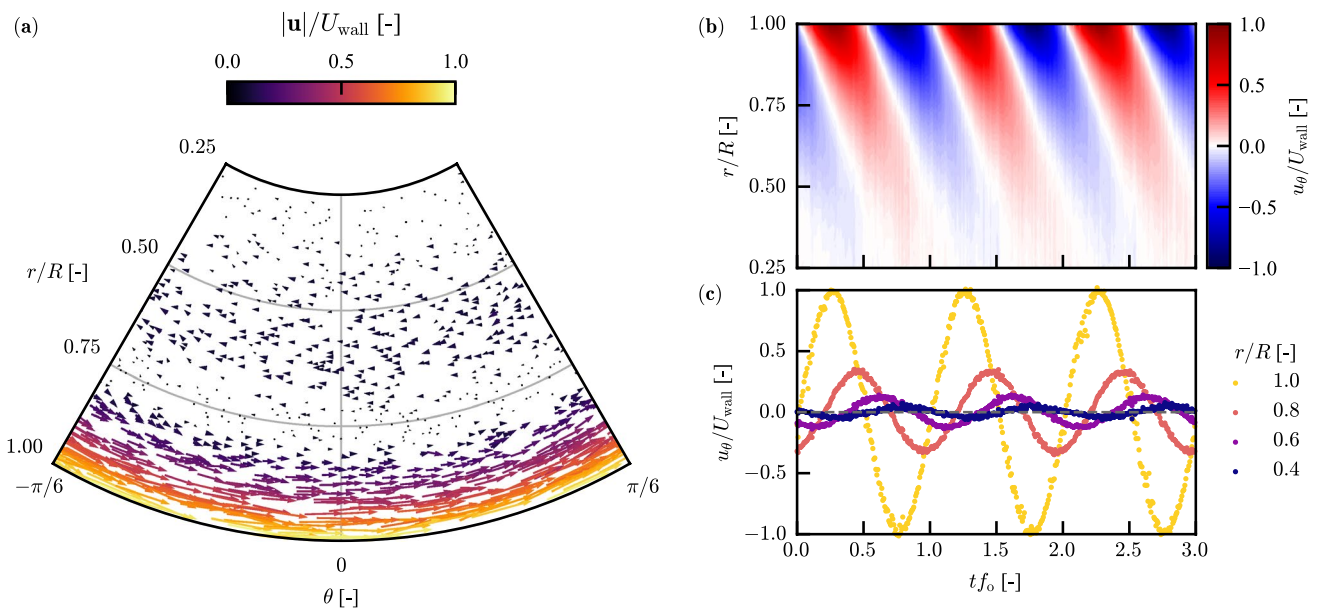

Fig. 3 Identified cylindrical wall and its center positions superposed on an inverted pathline image. An enlarged view of the region surrounded by the blue square is shown in the inset

Fig. 4 An example of $u_\theta(r, t)$ acquisition for 85-wt.% GS at $T = 25°C$ measured with $f_{\mathrm{o}} = 0.1$ Hz and $\Theta = \pi/3$: **a** an instantaneous velocity vector field measured by PTV at a moment $u_{\mathrm{wall}}(t) \approx U_{\mathrm{wall}}$ ($tf_{\mathrm{o}} \approx 0.25$), **b** a spatiotemporal map of the azimuthally averaged azi-

muthal velocity $u_\theta(r, t)$, and **c** sinusoidal temporal signals of $u_\theta(r, t)$ at different radial positions extracted from **b**. All the data points are reduced from the original number of data points for better visibility

be obtained using standard differential schemes. In Fig. 4, an example of $u_\theta(r,t)$ acquisition based on PTV is shown for the case of an 85-wt.% glycerol solution (GS) at $T = 25°C$. This measurement was done with parameters of $f_o = 0.1$ Hz and $\Theta = \pi/3$. The original scattered velocity vectors of tracer particles shown in Fig. 4a are interpolated using Eq. 6, and time series of $u_\theta(r;t)$ can be mapped into a spatiotemporal map $u_\theta(r,t)$ (Fig. 4b). Here, the thickness of the concentric region for the interpolation is $\Delta r = 1$ mm (Eq. 6) , and the $u_\theta(r,t)$ map is interpolated at every 0.5 mm in the radial direction. Examples of sinusoidal signals $u_\theta(t;r)$ extracted from Fig. 4b are shown in Fig. 4c. The amplitude imposed at the sidewall gradually decays as going to the internal region and propagates with a phase lag $\phi_e(r)$.

Once $u_\theta(r,t)$ is obtained, the amplitude and the phase lag distributions, $U_e(r)$ and $\phi_e(r)$, can be derived through the least-squares fit using a sinusoidal signal

$$u_\theta(t; r) = U_e(r) \sin\left[2\pi f_o t + \phi_e(r)\right] \tag{7}$$

at each radial position. After deriving the phase lag at all the radial positions, it is differentiated using the central difference scheme to obtain the $\phi'_e(r) = d\phi_e(r)/dr$. Examples of the amplitude and the phase lag gradient distributions, $U_e(r)$ and $\phi'_e(r)$, are shown in Fig. 5a and b. It is possible to identify an exponential decay of the $U_e(r)$ in Fig. 5a. The $\phi'_e(r)$ is almost constant along the radius in Fig. 5b, meaning the phase lag propagates at a constant rate, typical for a Newtonian fluid.

The phase lag gradient, $\phi'_e(r)$, is then compared with those of the sets of the analytic solutions for Newtonian fluids with varying ν. The effective kinematic viscosity $\nu_{eff}(r)$ is obtained as ν satisfying $\phi'_e(r) = \phi'(r;\nu)$ at each radial position. In Fig. 5c, the $\nu_{eff}(r)$ is plotted. While a slight change in the radial

direction is recognizable, the distribution of $\nu_{eff}(r)$ is almost flat across the whole region.

To obtain viscosity curves, it is a must to acquire shear rate $\dot{\gamma}(r,t)$ corresponding to the viscosity determined locally. The simple shear rate $\dot{\gamma}(r)$ in the axisymmetric and unidirectional flow is written as

$$\dot{\gamma}(r,t) = \left(\frac{\partial}{\partial r} - \frac{1}{r}\right) u_\theta(r,t). \tag{8}$$

Substituting Eq. 7 into Eq. 8, a periodic change of shear stress at r is derived as

$$\begin{aligned}\dot{\gamma}(r,t) &= \left(\frac{\partial}{\partial r} - \frac{1}{r}\right) U_e(r) \sin\left[2\pi f_o t + \phi_e(r)\right] \\ &= \dot{\gamma}_{max}(r) \sin\left[2\pi f_o t + \phi_e(r) + \psi_e(r)\right],\end{aligned} \tag{9}$$

where $\dot{\gamma}_{max}(r)$ is the maximum shear rate achieved at the radial position,

$$\dot{\gamma}_{max}(r) = \sqrt{\left[\left(\frac{d}{dr} - \frac{1}{r}\right) U_e(r)\right]^2 + \left[U_e(r)\frac{d}{dr}\phi_e(r)\right]^2}, \tag{10}$$

and an additional phase lag for the shear rate $\psi_e(r)$ is obtained as

$$\psi_e(r) = \tan^{-1}\left[\frac{U_e(r)\dfrac{d}{dr}\phi_e(r)}{\left(\dfrac{d}{dr} - \dfrac{1}{r}\right) U_e(r)}\right]. \tag{11}$$

Since $\dot{\gamma}(r,t)$ is a sinusoidal signal at each radial position, the effective shear rate $\dot{\gamma}_{eff}(r)$ is computed as

$$\dot{\gamma}_{eff}(r) = \sqrt{f_o \int_0^{1/f_o} \dot{\gamma}^2(r,t)dt} = \frac{1}{\sqrt{2}}\dot{\gamma}_{max}(r). \tag{12}$$

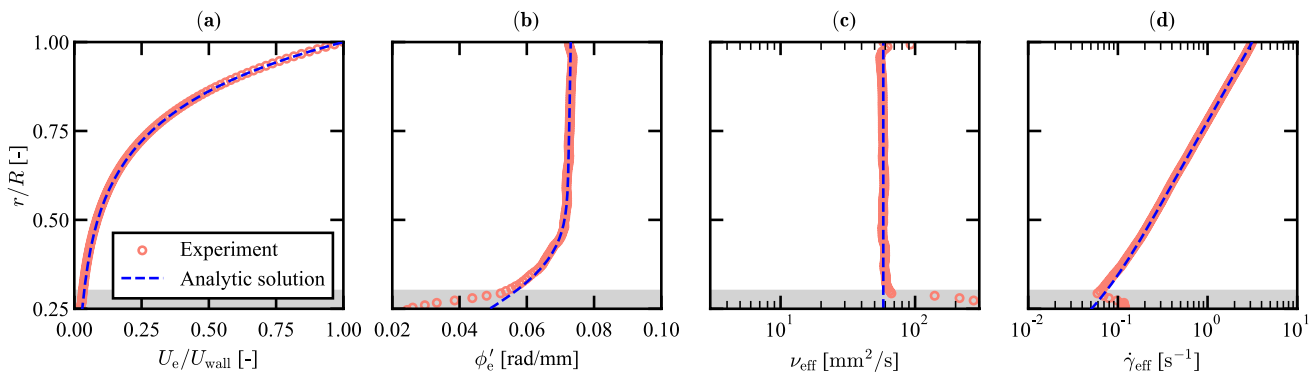**Fig. 5** Radial distributions of physical quantities obtained throughout the spinning rheometry for the case of 85-wt.% GS at $T = 25°C$ measured with $f_o = 0.1$ Hz and $\Theta = \pi/3$: **a** Velocity amplitude U_e, **b** phase lag gradient ϕ'_e, **c** effective kinematic viscosity ν_{eff}, and **d** shear rate $\dot{\gamma}_{eff}$. Dashed lines are the analytic solution for $\nu = 58$ mm^2/s, corresponding to the mean kinematic viscosity of this fluid. Gray highlighted regions, $r < 0.3R$, is the region not used for the later analysis due to lack of velocity information

A practical example of the effective shear rate distribution $\dot{\gamma}_{\text{eff}}(r)$ is shown in Fig. 5d, and it becomes smaller as it departs from the cylindrical wall.

Consequently, the radial distributions of $\nu_{\text{eff}}(r)$ and $\dot{\gamma}_{\text{eff}}(r)$ are obtained from the experimentally measured $u_\theta(r, t)$ as shown in Fig. 5c and d. Associating these two values at each radial position, the shear-rate-dependent viscosity curves $\nu_{\text{eff}}(\dot{\gamma}_{\text{eff}})$ can be acquired.

2.4 Assessment of measurement limitations and measurable ranges

To implement the OSR, one needs to pay attention to the limitations and applicable ranges. Since the OSR and other kinematic rheometry rely on specific assumptions, there are several requirements to fulfill, and the dynamic ranges of the kinematic viscosity and the shear rate which can be measured by the OSR must be known before the application in order to acquire proper viscosity curves. Similar discussions about the limitations and measurable ranges of the USR and those of an in-line pipe rheometry system can be found, respectively, in Yoshida et al. (2022) and Tasaka et al. (2021). While the OSR can measure shear-rate-dependent kinematic viscosity of both Newtonian and non-Newtonian fluids, it may be hard to discuss limitations for non-Newtonian fluids, which have a variety of material properties. Hence, the limitations and applicable ranges of the OSR are discussed in the following section by assuming a fluid of representative kinematic viscosity ν.

2.4.1 Limitations in kinematic viscosity ν

The applicable range of the OSR in terms of the kinematic viscosity ν is the primary interest to be explained in detail for a proper selection of the test fluid. The thickness of the viscous layer δ_ν controlled by the oscillation frequency f_{o} (Eq. 5) plays an important role in this measurement, and it must fulfill the requirements arising from the measurement system. First, the viscous layer should be thicker than the spatial resolution of the system, i.e., $\delta_\nu > d_{\text{p}}$. This condition determines the lower limit of the measurable kinematic viscosity as the spatiotemporal map of the azimuthal velocity $u_\theta(r, t)$ needs to resolve the viscous layer. Otherwise, the phase lag gradient $\phi'_{\text{e}}(r)$ cannot be obtained from the measurements based on PTV. Second, the upper limit of the viscous layer thickness is determined to ensure the system contains viscosity information in the velocity field. Since the viscosity information appears as the phase lag and its gradient, it is impossible to derive viscosity from a rigid-body rotation. Accordingly, the viscous layer needs to be thinner than the radius, i.e., $\delta_\nu < R$; otherwise, the rigid-body rotation develops immediately during the oscillation cycle. In addition, the particle diameters d_{p} need to be paid attention to, especially when measuring non-Newtonian fluids. Since

d_{p} is the minimum measurement volume in PTV, it should be sufficiently larger than the length scale of the molecular structures of the non-Newtonian fluids λ, that is $d_{\text{p}} \gg \lambda$. For the cases of polymer solutions, the size of the molecular structures is in the order of nanometers, and small particles with $d_{\text{p}} \sim \lambda$ cannot be utilized as seeding particles. This is because such tiny particles do not provide intense enough light for the wavelength of the laser illumination λ_{L} due to the limitation of the Mie scattering, $d_{\text{p}} \gg \lambda_{\text{L}}$ (Tropea et al. 2007). Thus, the limit for d_{p} does not matter in a standard PTV configuration. Summarizing above, the viscous layer thickness δ_ν needs to satisfy the relationship

$$\lambda \ll d_{\text{p}} < \delta_\nu < R. \tag{13}$$

In terms of ν, Eq. 13 is rewritten as

$$\pi d_{\text{p}}^2 f_{\text{o}} < \nu < \pi R^2 f_{\text{o}} \tag{14}$$

from Eq. 5. In Fig. 6a, the measurable ranges of ν are plotted as a function of f_{o} for different cylinder radii R and particle diameters d_{p}. The solid lines are the limitations in the present study, and the measurable range is colored gray. The dashed lines represent the limitations arising when different geometries are used for the OSR. For a less viscous fluid, it is necessary to apply a small oscillation frequency f_{o}. For a viscous fluid, f_{o} needs to be set higher or the cylindrical system needs to be larger to satisfy Eq. 13. It is noteworthy that the measurable range of ν is independent of shear stress τ imposed on the test domain and is only determined by the geometrical parameters R and d_{p}, as the OSR is independent of torque sensors.

2.4.2 Limitations in wall velocity U_{wall}

Since the wall velocity U_{wall} is the maximum velocity in the system, U_{wall} needs to be set carefully within a certain range. The two control parameters, f_{o} and Θ, set the wall velocity U_{wall}, and an axisymmetric and unidirectional flow should be ensured with the U_{wall}. This requirement determines the upper limit of U_{wall}, as the method assumes laminar flows without any secondary flows, such as Görtler vortices (Saric 1994). The Görtler number G, a product of boundary layer Reynolds number and wall curvature, is often defined as

$$G = \frac{U_{\text{wall}} \delta_\nu}{\nu} \sqrt{\frac{\delta_\nu}{R}}. \tag{15}$$

Considering the critical Görtler number G_{c} for the onset of Görtler vortices, the upper limit for the selection of the U_{wall}, as well as f_{o} and Θ is found, i.e., $G < G_{\text{c}}$. In practice, $G_{\text{c}} = 10$ is taken for the critical value, and the maximum velocity U_{max} can be varied before the onset. Please note that this upper limit for U_{wall} overestimates the onset of the
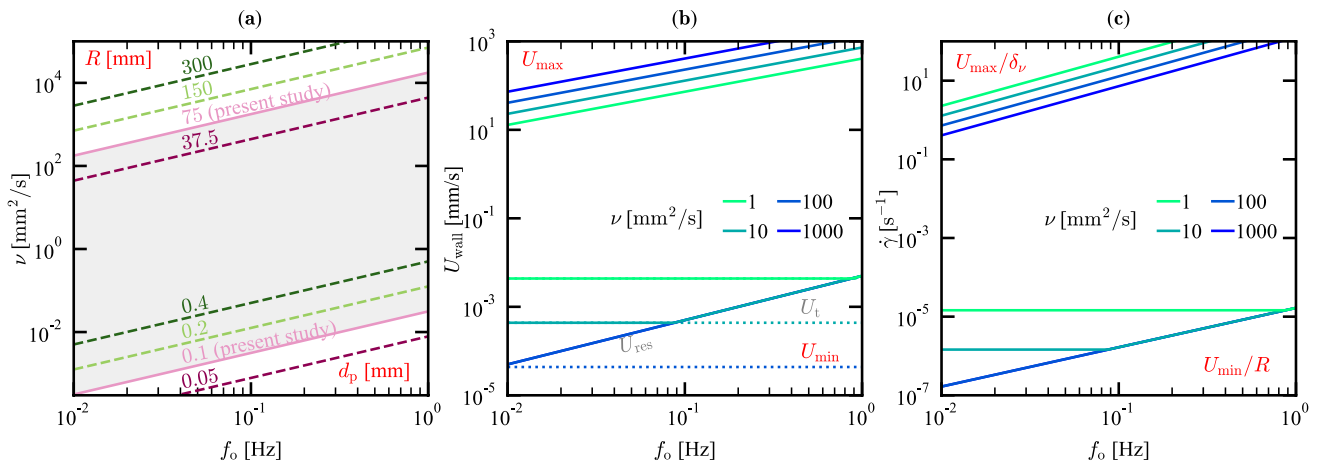
Fig. 6 Relationship of oscillation frequency f_o and other parameters: **a** kinematic viscosity ν for different geometries R and d_p, **b** the wall velocity U_{wall} can be set with $G_c = 10$ for different ν, and **c** the shear rate limitations $\dot{\gamma}$ for different ν in the present system ($R = 75$ mm). Solid and dashed lines in **a** show the present conditions ($R = 75$ mm and $d_p = 0.1$ mm) and other typical conditions for reference, and the gray region shows the measurable range of the present study. Solid lines in **b** indicate U_{max} (top) and U_{min} (bottom), and dotted lines are U_t for different ν. Upper limitations and lower limitations of $\dot{\gamma}$ are represented by solid lines in **c** in the same manner as **b** for different ν

secondary flow . The oscillatory forcing may suppress the growth of instability continuously , i.e., the secondary flow may not emerge at the limit, as G_c is originally derived for steady rotation. In the present study, we did not observe secondary flows at higher U_{wall} specified here and confirmed that all the conditions satisfy the assumptions.

Meanwhile, the lower limit U_{min} might be constrained due to the necessity of seeding particles. Even if ideal flow conditions are met by satisfying Eq. 13 with $G < G_c$, it is not possible to avoid the density difference between the seeding particles and the test fluids. In practice, the tracer particles are not neutrally buoyant and definitely settle or float at the Stokes (terminal) velocity U_t. Assuming the Stokes law is held, U_t for a spherical particle is estimated as

$$U_t = \frac{g d_p^2 |\rho - \rho_p|}{18 \rho \nu}, \tag{16}$$

where g and ρ are the gravity acceleration and the density of the fluid, respectively (Clift et al. 2005). In the present experiments, the terminal velocity orients the z-axis (gravitational axis), and the sedimentation and the flotation of the particles may cause pseudo-axial velocity and azimuthal velocity components can be no longer significant. Thus, U_{wall} needs to be sufficiently larger than the pseudo-axial flow, i.e., $U_{wall} \gg U_t$. Although Eq. 16 provides an estimate of the terminal velocity, it is strongly recommended to directly assure the U_t in the actual setup as it reflects characteristics of each seeding particle, such as actual diameter and density. In the present study, U_t was in $O(10^{-3}$ mm/s) for the worst case (water), which was small enough to obtain meaningful velocity information induced by the oscillating wall.

In addition to the discussion on U_t, it is worth noting the time resolution of the system, which is another factor determining the velocity limitation. The minimum velocity that can be measured by PTV, i.e., the velocity resolution, is

$$U_{res} = \frac{\alpha \Delta P_{min}}{\Delta t_{max}} \tag{17}$$

where α is the spatial resolution of the digital image in units of mm /pixel , and ΔP_{min} is the minimum image displacement detectable by PTV. Typically, $\alpha = 0.1$ mm/pixel in the present configuration, and $\Delta P_{min} = 0.1$ pixel, meaning subpixel . The remaining Δt_{max} is the maximum time interval between the two consecutive images. Please note that Δt_{max} cannot be infinity to capture almost zero velocity, and it is strictly determined from the Nyquist frequency f_N of the oscillatory system because the present method imposes a sinusoidal signal at the wall. To sample the velocity signal as a proper sinusoidal form, the two consecutive images used for PTV analysis need to be sampled at a higher frame rate than $f_N = f_o/2$; otherwise , the sinusoidal signals will collapse due to the aliasing effect. The maximum time interval is thus $\Delta t_{max} = 2/f_o$, and namely, the detectable minimum velocity (velocity resolution) is uniquely determined as

$$U_{res} = \frac{\alpha \Delta P_{min} f_o}{2}. \tag{18}$$

Depending on the parameter setting for the OSR and the kinematic viscosity, the minimum velocity U_{min} can be either U_t or U_{res}, and U_{wall} must exceed both of them.

Incorporating the discussion above, the wall velocity U_{wall} needs to be set while satisfying the following relation,

$$U_{\min} < U_{\text{wall}} < \pi^{3/4} G_c R^{1/2} \nu^{1/4} f_o^{3/4}, \tag{19}$$

where

$$U_{\min} = \max(U_t, U_{\text{res}}). \tag{20}$$

In Fig. 6b, the limitations of U_{wall} for the present geometry are drawn as functions of f_o for different ν. The lines at the top are $U_{\max}$ and those at the bottom are $U_{\min}$. The inclined line at the bottom corresponds to U_{res}, and the horizontal dotted lines are U_t. The range is smaller for smaller kinematic viscosity.

As U_{wall} is defined using the two independent parameters f_o and Θ, the maximum amplitude $\Theta_{\max}$ is also found as

$$\Theta_{\max} = \frac{G_c \nu^{1/4}}{2\pi^{1/4} R^{1/2} f_o^{1/4}} \tag{21}$$

for a given ν and f_o. An advantage of the OSR is that the derivations of local viscosity and shear rate described in Sect. 2.3 can be done independently at each radial position. Thanks to this, the whole domain needs not to be analyzed with the same PTV parameters, and this allows adjusting the time interval of PTV Δt at each radial position in order to set an optimal dynamic range of velocity at the position. Thus, the full range of the velocity (Eq. 19) is accessible using an identical optical system.

2.4.3 Limitations in shear rate $\dot{\gamma}$

The discussions above consider the application of the proposed method by keeping proper assumptions arising both in terms of theoretical and experimental basis. The range of the shear rate $\dot{\gamma}$ is then automatically determined using the maximum and minimum values of the velocities, $U_{\max}$ and $U_{\min}$, and those of the length scales, $\ell_{\min}$ and $\ell_{\max}$, in the measurement system. Hence, the shear rate range of the OSR is written as

$$\frac{U_{\min}}{\ell_{\max}} \lesssim \dot{\gamma} \lesssim \frac{U_{\max}}{\ell_{\min}}. \tag{22}$$

The $U_{\max}$ is identical to U_{wall} set in the range described in Eq. 19. As specified in Eq. 20, the $U_{\min}$ can be either U_t (Eq. 16) or U_{res} (Eq. 18), and it depends on the system configuration. The length scales are estimated as $\ell_{\max} = R$ and $\ell_{\min} = \delta_\nu$. As such, the range of the shear rate Eq. 22 can be rewritten using Eqs. 5 and 19 as

$$\frac{U_{\min}}{R} \lesssim \dot{\gamma}_{\text{eff}} \lesssim \frac{U_{\max}}{\delta_\nu} = \frac{\pi^{5/4} G_c R^{1/2} f_o^{5/4}}{\nu^{1/4}}. \tag{23}$$

Note that the maximum shear rate can be underestimated due to the underestimation of the maximum velocity as discussed in Sect. 2.4.2.

In Fig. 6c, the measurable range of the shear rate in the present study ($R = 75$ mm) is shown for different kinematic viscosity cases. By varying f_o, the shear rate can be measured up to $O(10^1–10^2 \text{ s}^{-1})$ depending on ν. For the lower limits, it lies roughly in $O(10^{-7}–10^{-5} \text{ s}^{-1})$. It is, however, not practical, as the density of the tracer particles cannot exactly match the fluids as stated above, especially when a less viscous fluid is tested. The terminal velocity U_t for the case of water ($\nu \approx 1 \times 10^{-6} \text{ m}^2/\text{s}$) is $O(10^{-5} \text{ m/s})$ if the density contrast of the fluid and the particles is 1%, and the system must measure velocity one or two order of magnitude higher than U_t. Hence, the minimum shear rate is practically in $O(10^{-3}–10^{-2} \text{ s}^{-1})$ with the present configuration. Even though the lower limits need to be estimated as higher than Eq. 23, this practical limit is incredibly low and can surpass that of the conventional torque-type rheometer (Nishinari et al. 2019).

3 Verification in Newtonian fluids

The performance of the OSR proposed in Sect. 2 is verified utilizing Newtonian fluids, as rich literature on their physical properties is available, and the results of the OSR can be directly compared with them. Here, three different Newtonian fluids, water, 85-wt.%, and 99-wt.% GSs, are employed as test fluids for verification. These three test fluids were selected to cover a wide range of kinematic viscosity, $\nu = O(10^0–10^3 \text{ mm}^2/\text{s})$ in a temperature range of $10°C \leq T \leq 40°C$, in order to show the capability of the present method. The temperature-dependent kinematic viscosity $\nu(T)$ was investigated by changing the temperatures of the circulating water in the rectangular tank in this range every 15°C, i.e., $T = 10, 25,$ and $40°C$.

In Fig. 7, kinematic viscosity curves of the three Newtonian fluids measured at $T = 25°C$ are shown. The analytic procedures for the case of 85-wt.% GS are already shown above in Figs. 4 and 5. Please note that the number of plots is reduced for the sake of visibility. Entirely, the measured values lie in the range of $\dot{\gamma}_{\text{eff}} = O(10^{-2}–10^1 \text{ mm}^2/\text{s})$ and $\nu_{\text{eff}} = O(10^0–10^3 \text{ mm}^2/\text{s})$. The plots for the three cases seem to be slightly inclined, yet they are effectively flat. In general, the kinematic viscosity of Newtonian fluids is independent of the shear rate, and thus, this can be identified using a power law model described as

$$\nu(\dot{\gamma}) = \frac{\mu(\dot{\gamma})}{\rho} = \frac{K}{\rho} \dot{\gamma}^{n-1}, \tag{24}$$

where K and n are constants, and n approaches to unity for a Newtonian fluid. Please note that the power law model (Eq. 24) is defined for kinematic viscosity unlike that defined for dynamic viscosity. Solid lines shown in Fig. 7 represent the power law fitting obtained from the experimental results,
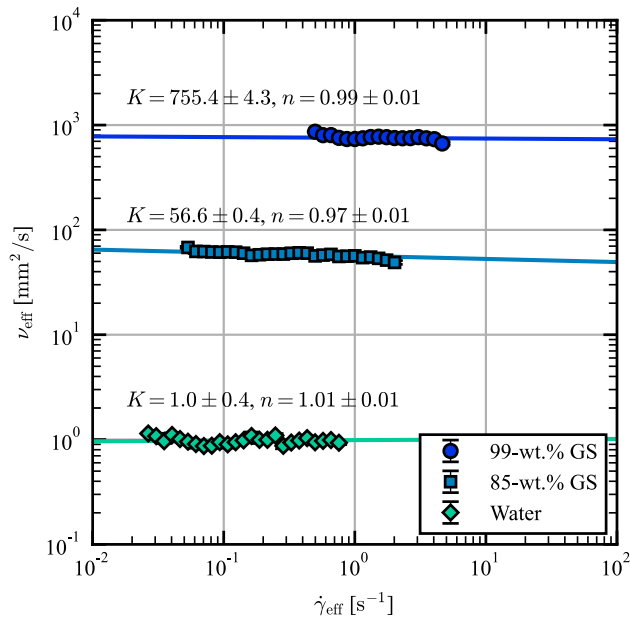
Fig. 7 Kinematic viscosity curves of Newtonian fluids, 99-wt.% GS ($f_o = 0.8$ Hz and $\Theta = \pi/3$), 85-wt.% GS ($f_o = 0.1$ Hz and $\Theta = \pi/3$), and water ($f_o = 0.04$ Hz and $\Theta = \pi/9$), at $T = 25°C$. Solid lines are the power-law fitting (Eq. 24), and the coefficients for the fitting are noted above each line. The number of plots is reduced from the originals for the sake of clarity

Fig. 8 Kinematic viscosity of Newtonian fluids, 99-wt.% GS, 85-wt.% GS, and water measured at different temperatures. Literature values drawn as solid lines are computed using density values by Bosart and Snoddy (1927) and viscosity values by Segur and Oberstar (1951). Error bars for the obtained data represent standard deviations in shear rate

and these constants are noted above each line with standard deviations. In this measurement, n values are almost unity for all three cases. The deviations from unity are expected due to inhomogeneity of the fluids, such as concentration and temperature. Considering this, the three test fluids can be regarded as Newtonian.

To show the validity of the present method, the kinematic viscosity of the three Newtonian fluids is compared with literature values. In Fig. 8, the kinematic viscosity measured at different temperatures is plotted. Here, the plotted values are the kinematic viscosity averaged over the whole shear rate range, and each error bar represents the standard deviation for it. The kinematic viscosity becomes smaller according to the increase in temperature for all the test fluids. The solid lines are the literature values for the three test fluids shown for comparison. Here, the temperature-dependent values of density $\rho(T)$ and dynamic viscosity $\mu(T)$ of the fluids are taken from the tables provided by Bosart and Snoddy (1927) and Segur and Oberstar (1951), respectively, to compute temperature-dependent kinematic viscosity $\nu(T) = \mu(T)/\rho(T)$. The measured kinematic viscosity shows good agreement with the literature values. It is noteworthy that the OSR provides stable performance irrespective of the magnitude of the kinematic viscosity. This is one of the benefits of the OSR that only utilizes velocity information measured by PTV. As above, the dynamic range of the velocity is easily tuned into an optimal range for the
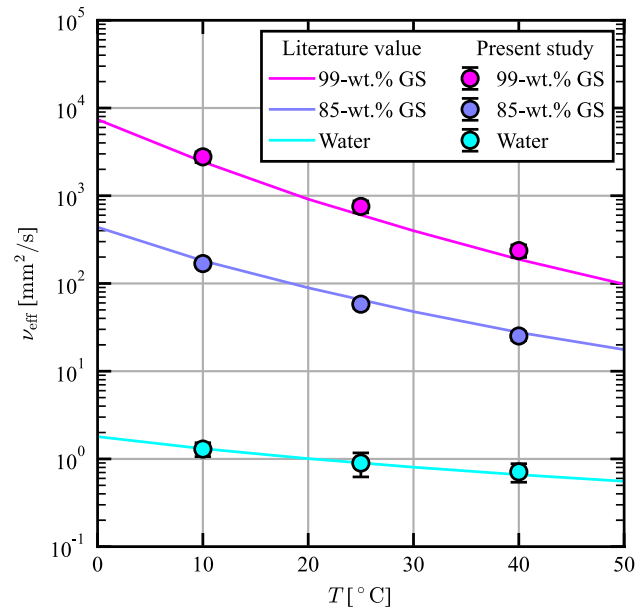
test fluids, and this enables measurement of kinematic viscosity at the same degree of relative errors in a wide range of kinematic viscosity.

4 Application to dilute polymer solutions

As an application, we demonstrate viscosity measurements of dilute polymer solutions to emphasize the capability of OSR in measuring less viscous non-Newtonian fluids. As the test fluids, we employed xanthan-gum solutions (XGS), which are the well-known shear-thinning fluids (e.g., Whitcomb and Macosko 1978). The concentrations of the XGSs were set $c = 0.04, 0.02,$ and 0.01 wt.%, which are remarkably dilute. In general, the XGSs are opaque liquids and are hard to apply optical methods like PIV/PTV. In this study, the dilute solutions enabled us to visualize tracer particles being brighter than the flare due to the opaqueness. Thus, PTV measurements were possible even at the highest concentration case, $c = 0.04$ wt.%. The kinematic viscosity curves of the XGSs measured at different temperatures, $T = 10°C,$ $25°C,$ and $40°C$ are shown, respectively, in Fig. 9a–c. For all the temperature conditions, the denser solution has higher kinematic viscosity over the whole shear rate range measured in the experiments. The kinematic viscosity values gradually decrease with the increase in temperature. The plots show both plateau and inclined regions, especially for
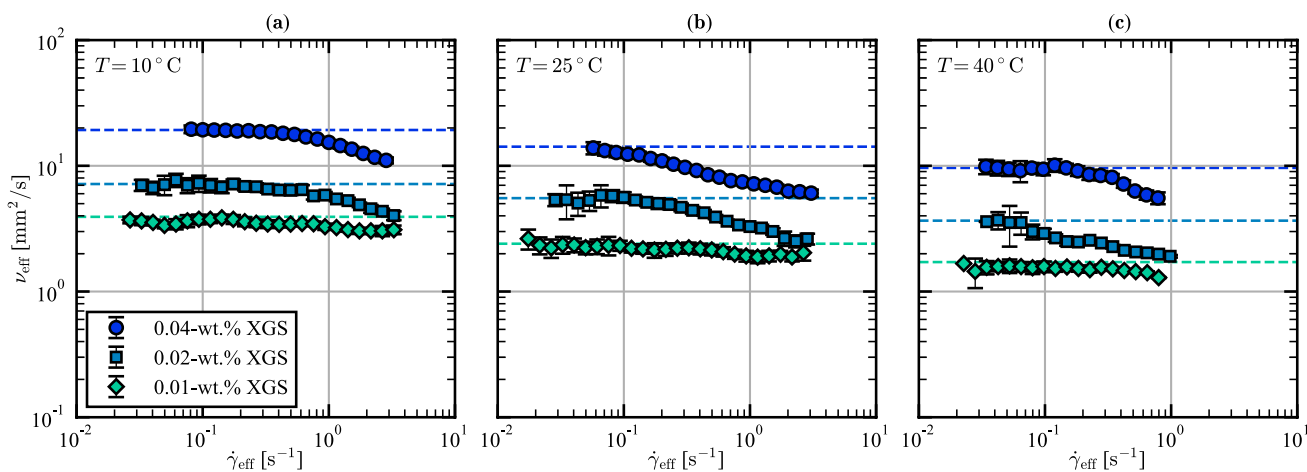
Fig. 9 Kinematic viscosity curves of XGSs measured at different temperatures: **a** $T = 10°C$, **b** $T = 25°C$, and **c** $T = 40°C$. Plots are reduced from the originals for the sake of clarity. Dashed lines are the estimated zero shear kinematic viscosity ν_0. All the conditions are measured with $f_o = 0.05$ Hz and $\Theta = \pi/6$

the higher concentration cases. Since the upper range of the shear rate is not wide enough, it is not possible to construct constitutive equations like the cross model or Carreau–Yasuda model from these kinematic viscosity curves. To widen the upper limit of the shear rate, a larger cylinder needs to be employed according to Eq. 23 , or the higher shear rate range can be measured by a standard torque-type rheometer complementarily. It is remarkable that the plots show the presence of plateau regions, meaning the first Newtonian regime, at the low shear rate region $\dot{\gamma}_{eff} < 1$ s^{-1}. The first Newtonian regimes are shifted as the increase in concentration c for each temperature condition. Due to the increase in c, the relaxation time of the fluid increases, and the shear rate at which the Weissenberg number (the ratio of elastic force to viscous force) is equal to unity decreases. This is in good agreement with the general explanation of shear-thinning fluids (Wagner et al. 2017). Thanks to the well-defined first Newtonian regime, we can easily estimate the zero shear kinematic viscosity ν_0 of the XGSs as shown by the horizontal dashed lines in Fig. 9. These values might be hard to measure using the conventional torque rheometer. Let's suppose that a cone-plate rheometer with a radius of 30 mm is employed. The required torque resolution is $O(1$ nN $\cdot$ m) to measure $\nu = 10$ mm^2/s (equivalent to $\mu = 10^{-2}$ Pa $\cdot$ s) at $\dot{\gamma} = 10^{-2}$ s^{-1} from Eq. 1. Considering that the lower limit of the torque measured by the rheometer is practically larger than its resolution (Ewoldt et al. 2015), the estimated torque resolution is too precise to measure with a torque sensor.

In Fig. 10, the zero shear viscosity μ_0 is plotted against the concentration c. Here, the zero shear dynamic viscosity of XGSs is obtained from the density and the estimated zero shear kinematic viscosity as $\mu_0 = \rho\nu_0$. Please note that the dynamic viscosity plotted at $c = 0.00$ wt.% is the viscosity of the solvent (water) μ_s. The zero shear viscosity of XGSs
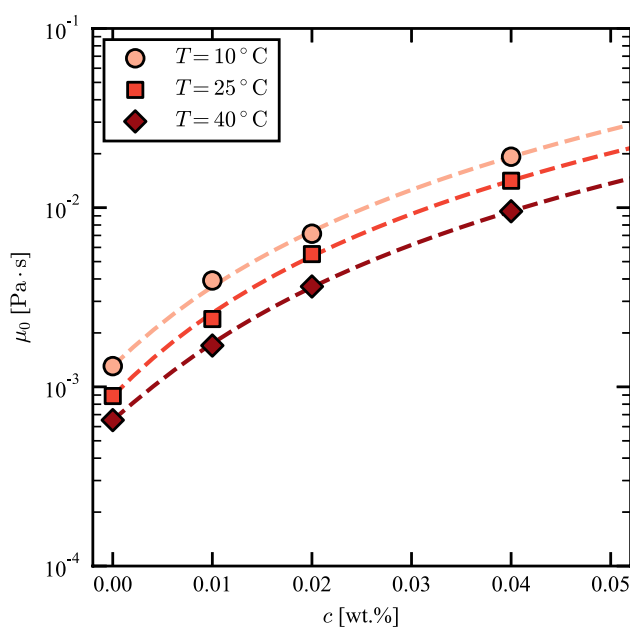
increases monotonically according to c for each temperature condition. For dilute polymer solutions, the specific viscosity $(\mu_0 - \mu_s)/\mu_s$ should follow the Huggins equation (Huggins 1942)

$$\frac{\mu_0 - \mu_s}{\mu_s c} = [\mu] + k_H[\mu]^2 c, \tag{25}$$

where $[\mu]$ is the intrinsic viscosity and k_H is the Huggins constant (Macosko 1994), and k_H ranges from 0.3 to 0.4 for

Fig. 10 Zero shear viscosity of XGSs μ_0 plotted against the concentration c. Dashed lines are the fittings by Eq. 25. The plots at $c = 0.00$ wt.% are the viscosity of water

good solutions. The least-squares fit using Eq. 25 are also shown in Fig. 10 as dashed lines. The plots regress well with the lines of Eq. 25, meaning that the estimated μ_0 represents proper material properties of dilute polymer solutions. Here, the two parameters are obtained as $[\mu] \approx 1.2 \times 10^2$ ml/g and $k_H \approx 0.36$ for all the temperature conditions, and these are reasonable results compared with the literature (Whitcomb and Macosko 1978; Huggins 1942). Incorporating all the results shown above, the established method, OSR, is capable of measuring material properties of dilute polymer solutions like zero shear viscosity and shear-thinning effects, even if the concentration is extremely low in $O(10$ ppm) without installing a precise torque sensor.

5 Summary and outlook

To expand the dynamic range of shear rate arising from the mechanical limitation of the conventional torque-type rheometer, a novel approach has been proposed building on the spinning rheometry introduced earlier by Tasaka et al. (2015). The method, termed optical spinning rheometry (OSR), is fully independent of torque measurements and utilizes velocity information measured by particle tracking velocimetry (PTV). The use of PTV and oscillating system increases the velocity resolution, and it benefits the exploration of low shear rate regions $O(\leq 10^{-1}$ s$^{-1})$ of the kinematic viscosity curves. Details of analytic procedures and limitations arising in measuring material properties are discussed carefully considering measurement characteristics of PTV and those of flow fields. The performance of the OSR is validated in Newtonian fluids, and the outcomes show a good agreement with the literature values. The OSR is also applied to dilute polymer solutions of $O(10$ ppm), and kinematic viscosity curves at low values $\nu = O(10^0$–10^2 mm^2/s) at low shear rate region, $\dot{\gamma} \leq O(10^{-1}$ s$^{-1})$ are successfully obtained.

The optical approach surpasses the limitation of conventional USR proposed earlier, and it enables measurements of rheological properties like pseudo-plastic of less viscous fluids at low shear rate regions. By altering the geometry of the experimental device, the measurable range of the shear rate and the kinematic viscosity can be further expanded as mentioned in Sect. 2.4. This allows us to construct constitutive equations of dilute or semi-dilute polymer solutions from the experimental data covering both the zero shear viscosity and the infinite shear viscosity. In addition, the rapid evaluation allows for measuring time-dependent rheological properties of test fluids, and the wide domain expands measurable fluids. Thus, complex fluids containing time-dependency and large length scales like bubbly liquids can also be measured as long as they are optically accessible. The constitutive equations built by actual materials will facilitate understanding of the non-Newtonian fluid dynamics from experimental as well as from analytical and numerical approaches.

Declarations

References

Abbasian M, Shams M, Valizadeh Z, Moshfegh A, Javadzadegan A, Cheng S (2020) Effects of different non-Newtonian models on unsteady blood flow hemodynamics in patient-specific arterial models with in-vivo validation. Comput Methods Programs Biomed 186:105185. https://doi.org/10.1016/j.cmpb.2019.105185

Alves M, Oliveira P, Pinho F (2021) Numerical methods for viscoelastic fluid flows. Annu Rev Fluid Mech 53:509–541. https://doi.org/10.1146/annurev-fluid-010719-060107

Barnes HA, Hutton JF, Walters K (1989) An introduction to rheology, vol 3. Elsevier, London

Bosart L, Snoddy A (1927) New glycerol tables[1]. Ind Eng Chem 19(4):506–510. https://doi.org/10.1021/ie50208a030

Clift R, Grace JR, Weber ME (2005) Bubbles, drops, and particles. Courier Corporation

Den Toonder J, Hulsen M, Kuiken G, Nieuwstadt F (1997) Drag reduction by polymer additives in a turbulent pipe flow: numerical and laboratory experiments. J Fluid Mech 337:193–231. https://doi.org/10.1017/S0022112097004850

Dimitriou CJ, McKinley GH, Venkatesan R (2011) Rheo-PIV analysis of the yielding and flow of model waxy crude oils. Energy Fuels 25(7):3040–3052. https://doi.org/10.1021/ef2002348

Dimitropoulos CD, Sureshkumar R, Beris AN, Handler RA (2001) Budgets of Reynolds stress, kinetic energy and streamwise enstrophy in viscoelastic turbulent channel flow. Phys Fluids 13(4):1016–1027. https://doi.org/10.1063/1.1345882

Escudier M, Nickson A, Poole R (2009) Turbulent flow of viscoelastic shear-thinning liquids through a rectangular duct: quantification of turbulence anisotropy. J Nonnewton Fluid Mech 160(1):2–10. https://doi.org/10.1016/j.jnnfm.2009.01.002

Ewoldt RH, Johnston MT, Caretta LM (2015) Experimental challenges of shear rheology: how to avoid bad data. In: Complex fluids in biological systems, Springer, pp 207–241

Huggins ML (1942) Theory of solutions of high polymers1. J Am Chem Soc 64(7):1712–1719

Hyun K, Wilhelm M, Klein CO, Cho KS, Nam JG, Ahn KH, Lee SJ, Ewoldt RH, McKinley GH (2011) A review of nonlinear oscillatory shear tests: analysis and application of large amplitude oscillatory shear (LAOS). Prog Polym Sci 36(12):1697–1753. https://doi.org/10.1016/j.progpolymsci.2011.02.002

Macosko CW (1994) Rheology principles. Measurements and Applications

Mader H, Llewellin E, Mueller S (2013) The rheology of two-phase magmas: a review and analysis. J Volcanol Geoth Res 257:135–158. https://doi.org/10.1016/j.jvolgeores.2013.02.014

Medina-Bañuelos EF, Marín-Santibáñez BM, Pérez-González J, Kalyon DM (2019) Rheo-PIV analysis of the vane in cup flow of a viscoplastic microgel. J Rheol 63(6):905–915. https://doi.org/10.1122/1.5118900

Min T, Yoo JY, Choi H, Joseph DD (2003) Drag reduction by polymer additives in a turbulent channel flow. J Fluid Mech 486:213–238. https://doi.org/10.1017/S0022112003004610

Nishinari K, Turcanu M, Nakauma M, Fang Y (2019) Role of fluid cohesiveness in safe swallowing. NPJ Sci Food 3(1):1–13. https://doi.org/10.1038/s41538-019-0038-8

Noto D, Tasaka Y, Murai Y (2021a) In situ color-to-depth calibration: toward practical three-dimensional color particle tracking velocimetry. Exp Fluids 62(6):1–13. https://doi.org/10.1007/s00348-021-03220-9

Noto D, Terada T, Yanagisawa T, Miyagoshi T, Tasaka Y (2021b) Developing horizontal convection against stable temperature stratification in a rectangular container. Phys Rev Fluids 6(8):083501. https://doi.org/10.1103/PhysRevFluids.6.083501

Ohie K, Yoshida T, Tasaka Y, Murai Y (2022) Effective rheology mapping for characterizing polymer solutions utilizing ultrasonic spinning rheometry. Exp Fluids 63(2):1–12. https://doi.org/10.1007/s00348-022-03382-0

Saric WS (1994) Görtler vortices. Annu Rev Fluid Mech 26(1):379–409. https://doi.org/10.1146/annurev.fl.26.010194.002115

Segur JB, Oberstar HE (1951) Viscosity of glycerol and its aqueous solutions. Ind Eng Chem 43(9):2117–2120. https://doi.org/10.1021/ie50501a040

Serrano-Aguilera J, Parras L, del Pino C, Rubio-Hernandez F (2016) Rheo-PIV of Aerosil® R816/polypropylene glycol suspensions. J Nonnewton Fluid Mech 232:22–32. https://doi.org/10.1016/j.jnnfm.2016.03.015

Shepard D (1968) A two-dimensional interpolation function for irregularly-spaced data. In: Proceedings of the 1968 23rd ACM National Conference, Association for Computing Machinery, New York, NY, USA, pp 517–524, 10.1145/800186.810616

Song Y, Rau MJ (2020) Viscous fluid flow inside an oscillating cylinder and its extension to Stokes' second problem. Phys Fluids 32(4):043601. https://doi.org/10.1063/1.5144415

Sureshkumar R, Beris AN, Handler RA (1997) Direct numerical simulation of the turbulent channel flow of a polymer solution. Phys Fluids 9(3):743–755. https://doi.org/10.1063/1.869229

Tasaka Y, Kimura T, Murai Y (2015) Estimating the effective viscosity of bubble suspensions in oscillatory shear flows by means of ultrasonic spinning rheometry. Exp Fluids 56(1):1–13. https://doi.org/10.1007/s00348-014-1867-5

Tasaka Y, Yoshida T, Rapberger R, Murai Y (2018) Linear viscoelastic analysis using frequency-domain algorithm on oscillating circular shear flows for bubble suspensions. Rheol Acta 57(3):229–240. https://doi.org/10.1007/s00397-018-1074-z

Tasaka Y, Yoshida T, Murai Y (2021) Nonintrusive in-line rheometry using ultrasonic velocity profiling. Ind Eng Chem Res 60(30):11535–11543. https://doi.org/10.1021/acs.iecr.1c01795

Tropea C, Yarin AL, Foss JF et al (2007) Springer handbook of experimental fluid mechanics, vol 1. Springer, Cham

Wagner CE, Barbati AC, Engmann J, Burbidge AS, McKinley GH (2017) Quantifying the consistency and rheology of liquid foods using fractional calculus. Food Hydrocoll 69:242–254

Whitcomb PJ, Macosko C (1978) Rheology of xanthan gum. J Rheol 22(5):493–505. https://doi.org/10.1122/1.549485

Yoshida T, Tasaka Y, Murai Y (2017) Rheological evaluation of complex fluids using ultrasonic spinning rheometry in an open container. J Rheol 61(3):537–549. https://doi.org/10.1122/1.4980852

Yoshida T, Tasaka Y, Tanaka S, Park H, Murai Y (2018) Rheological properties of montmorillonite dispersions in dilute NaCl concentration investigated by ultrasonic spinning rheometry. Appl Clay Sci 161:513–523. https://doi.org/10.1016/j.clay.2018.05.017

Yoshida T, Tasaka Y, Murai Y (2019) Efficacy assessments in ultrasonic spinning rheometry: linear viscoelastic analysis on non-Newtonian fluids. J Rheol 63(4):503–517. https://doi.org/10.1122/1.5086986

Yoshida T, Ohie K, Tasaka Y (2022) In situ measurement of instantaneous viscosity curve of fluids in a reserve tank. Ind Eng Chem Res 61(31):11579–11588. https://doi.org/10.1021/acs.iecr.2c01792